Journal Pre-proofs

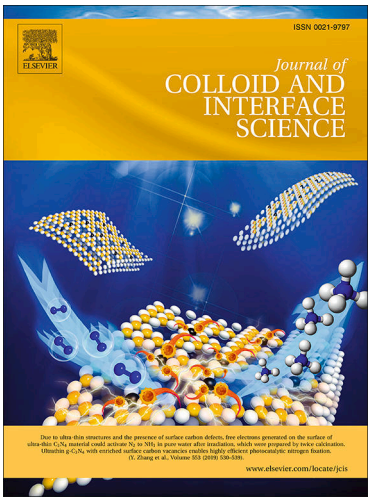

Preparation of P-g-C_3N_4-WS_2 nanocomposite and its application in photoelectrochemical detection of 5-formylcytosine

Fei Li, Huanshun Yin, Yan Chen, Siyu Wang, Jingyan Li, Yuemei Zhang, Chunxiao Li, Shiyun Ai

PII: S0021-9797(19)31311-6
DOI: https://doi.org/10.1016/j.jcis.2019.10.117
Reference: YJCIS 25611

To appear in: *Journal of Colloid and Interface Science*

Received Date: 30 August 2019
Revised Date: 31 October 2019
Accepted Date: 31 October 2019

Please cite this article as: F. Li, H. Yin, Y. Chen, S. Wang, J. Li, Y. Zhang, C. Li, S. Ai, Preparation of P-g-C_3N_4-WS_2 nanocomposite and its application in photoelectrochemical detection of 5-formylcytosine, *Journal of Colloid and Interface Science* (2019), doi: https://doi.org/10.1016/j.jcis.2019.10.117

Preparation of P-g-C_3N_4-WS_2 nanocomposite and its application in photoelectrochemical detection of 5-formylcytosine

Fei Li, Huanshun Yin*,Yan Chen, Siyu Wang, Jingyan Li, Yuemei Zhang, Chunxiao Li, Shiyun Ai

College of Chemistry and Material Science, Shandong Agricultural University, Taian 271018, P.R. China.

* Corresponding author.

E-mail: yinhs@sdau.edu.cn (Huanshun Yin).

Abstract: DNA formylation (5-formylcytosine, 5fC) is a major epigenetic modification involved in alterations in the DNA double helix structure and protein identification. Due to the low amount in all mammalian tissues and cells, it is necessary to develop a rapid, sensitive and efficient method for detecting 5fC for further understanding the biological functions of 5fC. Thus, a novel PEC biosensor was constructed using P-g-C_3N_4-WS_2 nanocomposite as photoactive material. Firstly, AuNPs/P-g-C_3N_4-WS_2/ITO electrode was prepared as substrate electrode. Secondly, the probe DNA and complementary DNA (containing 5fC base) was modified to the electrode surface based on the formation of Au-S bonds between AuNPs and thiol group on the probe DNA and hybridization, respectively. Finally, the amino functionalized MnO_2 nanoflowers were further modified to the electrode surface by covalent interaction between the aldehyde group on the 5fC and the amino group on MnO_2 nanoflowers. The sensitive and specific detection of 5fC can be achieved by oxidizing ascorbic acid with MnO_2 nanoflowers and quenching the photoactivity of P-g-C_3N_4-WS_2 nanocomposite. The sensor has a detection range of 0.01-200 nM and a detection limit of 3.8 pM. Moreover, this sensor has excellent detection specificity, stability and reproducibility.

Keywords: Protonated g-C_3N_4 nanosheets; WS_2 nanosheets; Heterojunction; Photoelectrochemical biosensor; DNA formylation; MnO_2 nanoflowers.

1. Introduction

5-Formylcytosine (5fC) is an important epigenetic modification, which has been found in various cellular genomic DNA and thought to be involved in the demethylation of DNA [1]. As an important intermediate oxidation product in the process of DNA demethylation, 5fC not only participates in gene regulation, cell differentiation, but also plays a vital role in human diseases [2]. Therefore, the analysis and detection of 5-formylcytosine helps to understand the biological processes associated with epigenetic modifications, providing a basis for clinical diagnosis and treatment. However, since 5-formylcytosine is oxidized by 5-hydroxymethylcytosine, so 5fC content in genomic DNA of mammalian cells only can be as low as 1/10 of 5-hydroxymethylcytosine [3], which is faced huge challenge. Thus, there is a need for a highly sensitive detection method to achieve detection of 5fC.

Photoelectrochemical (PEC) biosensors have become one of the most important research fields of modern biotechnology due to low cost and good sensitivity [4-7]. PEC biosensors combine electrochemical and optical technique with biosensing to achieve the high detection sensitivity, where the photocurrent change generated before and after the biometric process and the concentration of the marker was then detected based on the photocurrent change. Interestingly, this technique relies heavily on the conversion properties of photoelectrochemically active materials [8]. In date, PEC detection methods have been widely used to detect various biomolecules, including N6-methyladenosine (m6A) [9], creatine kinase-MB (CK-MB) [10], protein kinase A [11], microRNAs [12], alpha-fetoprotein [13], myoglobin [14], etc. Therefore, PEC

biosensor may be a good platform for detecting 5fC. To the best of our knowledge, no one currently uses PEC technique for 5fC detection.

In PEC analysis, two key factors are necessary: photoelectrically active substance (generating PEC signal) and biometric component. Photoactive materials are one of the important factors for PEC biosensor, which can greatly affect the sensitivity of PEC analysis technique. Thus, it is important to prepare photoactive materials with high photoelectric intensity [15, 16]. Currently, two-dimensional nanomaterials (e.g. g-C_3N_4, MoS_2, WS_2) are considered as good photoactive materials with good application prospect due to their excellent electrical, optical and photocatalytic properties [17-19]. Among them, tungsten sulfide (WS_2) has attracted a lot of interest in PEC biosensing due to its excellent visible light absorption capacity and high electron mobility [20]. However, WS_2 has a faster recombination rate of photogenerated electron-holes and is inherently poor in conductivity, which limits its application in PEC sensors. In order to overcome the above shortcomings, many studies have focused on recombining WS_2 with other semiconductor materials, which can effectively suppress the recombination rate of electron-hole pairs and accelerate the electron transmission [21, 22]. Notably, graphitic carbon nitride (g-C_3N_4), as a kind of metal-free two-dimensional semiconductor material, has also attracted more attentions due to the advantages of high surface active sites, visible light absorption, and good biocompatibility [23]. Considering the band gap relationship, g-C_3N_4 and WS_2 can be combined to increase the surface area and effectively accelerating the separation efficiency of carriers [24, 25]. Besides, manganese dioxide (MnO_2), as one of the excellent transition metal oxides,

has been widely used in the fields of molecular adsorption, catalysis, supercapacitors and electrochemistry. Due to its strong oxidation ability, MnO_2 can also be applied in PEC detection system to oxidize the electron donor in detection buffer, which will decrease the photocurrent of the photoactive material [26].

In addition to photoactive materials, the recognition of target molecule is also critical for PEC biosensor. Notably, 5fC has a unique aldehyde functional group, which is different from other cytosine derivatives (such as 5-methylcytosine and 5-hydroxymethylcytosine). In this way, the specific recognition of 5fC can be achieved based on aldehyde-specific reagent with relatively mild covalent reaction conditions, including hydrazine, amine, hydroxylamine, hydrazine, phenylenediamine amidoxyl and indole, etc [27, 28]. However, it is reported that amines have the advantage of being more stable and easier to synthesize than other materials, and that the active amine can directly label 5fC without any catalyst. Therefore, the amine may be a better reagent for recognizing 5fC.

Herein, a sensitive PEC biosensor was prepared to quantitatively detect 5fC with the advantages of enzyme-free and antibody-free, which not only greatly reduces the detection cost, but also improves the stability of the sensor. In this PEC biosensor, P-g-C_3N_4-WS_2 nanocomposite was employed as photoactive material, amino functionalized MnO_2 (MnO_2-NH_2) nanoflowers was used as PEC signal inhibitor, and the 5fC was recognized by the covalent reaction between amino group on MnO_2 and aldehyde group on 5fC.

2. Experimental section

2.1 Reagents and instruments

Melamine, chloroauric acid tetrahydrate ($HAuCl_4 \cdot 4H_2O$), sodium citrate, aminopropyltrimethoxysilane (APTES), oleic acid, toluene, $KMnO_4$, ascorbic acid (AA), poly(acrylic acid) and H_2SO_4 were ordered from Aladdin (Shanghai, China). N-(3-Dimethylaminopropyl)-N ′ -ethylcarbodiimide hydrochloride (EDC) and Nhydroxysuccinimide ester (NHS) were purchased by Macklin (Shanghai, China). 6-Mercapto-1-hexanol (MCH) and tungsten disulfide powder (WS_2) were obtained from Sigma-Aldrich (USA). DNA sequences were provided by Sangon (Shanghai, China). The DNA sequences are as follows: 5′-CGC GCG TAC ATC GGC CAC ATC T-SH-3 ′ (probe DNA); 5 ′ -AGA TGT GGC CGA TGT ACG CfGC G-3 ′ (complementary formylated DNA, 5fC-DNA); 5′-AGA TGT GGC CGA TGT ACG ChmGC G-3′ (complementary hydroxymethylated DNA, 5hmC-DNA); 5′-AGA TGT GGC CGA TGT ACG CmGC G-3′ (complementary methylated DNA, 5mC-DNA); 5′-AGA UGU GGC CGA UGU ACG CmGC G-3′ (complementary methylated RNA, 5mC-RNA).

The buffer solutions used is configured as follows: PEC detection buffer, 10 mM Tris-HCl containing 10 mM AA (pH = 7.4). EIS detection buffer, 10 mM Tris-HCl containing 5 mM $K_3[Fe(CN)_6]$, $K_4[Fe(CN)_6]$ and 0.1 mM KCl (pH = 7.4). Probe DNA immobilization buffer, 10 mM Tris-HCl, 1.0 M NaCl, 1.0 mM EDTA and 1.0 mM TCEP (pH = 7.4). DNA hybridization buffer, 10 mM Tris-HCl containing 1.0 mM EDTA, and 1.0 M NaCl (pH = 7.4). Washing buffer, 10 mM Tris-HCl containing 50 mM NaCl (pH = 7.4). All reagents and solutions (except for purchase) need to be

configured with autoclaved water. The tips and centrifuge tubes should be sterilized before use. PEC measurement was carried out on CHI832A electrochemical workstation (Austin, USA) equipped with 500 W Xe lamp as the irradiation source. Electrochemical impedance spectroscopy (EIS) measurement was performed on CHI660C electrochemical workstation (Austin, USA), covering the frequency range of 0.1 Hz - 100 kHz at a potential of 0.2 V.

Scanning electron microscopy (SEM) image was collected on a Zeiss Sigma 300 (Germany). The powder X-ray diffractometer (XRD) was performed on a Smartlab SE equipment operated at 40 kV and 30 mA (Rigaku, Japan). Atomic force microscope (AFM) was applied on a Bruker Dimension Icon equipment to scan samples in air using tapping mode (USA). Transmission electron microscopy (TEM) was obtained by FEI Tecnai G2 F20 (USA) emission transmission electron microscope at 220 kV. Fourier Transform Infrared (FT-IR) spectrum was received by Bruker Tensor Ⅱ (Germany).

2.2 Preparation of WS_2 nanosheets and protonated g-C_3N_4 (P-g-C_3N_4) nanosheets

WS_2 nanosheets were prepared using ultrasonic-assisted liquid-phase exfoliation technique according to previous work [29], where bulk WS_2 powder was employed as a raw material, PAA as exfoliating reagent and water as a solvent. Briefly, bulk WS_2 powder (1.5 g) and PAA (420 μL) were added into 20 mL of sterilized water and the mixture was sonicated for 8 h. Then, the dispersion was centrifuged at 3000 rpm for 10 min and the upper dark green layer was collected, which was further centrifuged at 10000 rpm for 10 min. The as-obtained black precipitate was washed for several times with water, and finally it was freezing dried in vacuum.

P-g-C_3N_4 was prepared according to the previous literature [30]. Firstly, graphitic carbon nitride (g-C_3N_4) was prepared by pyrolysis of melamine. In brief, 2 g melamine was placed in a porcelain boat with a lid, and then it was put into the center region of tube furnace. Afterwards, the tube furnace was heated in air from room temperature to 520 °C at a heating rate of 5 °C min^{-1}, and kept at 520 °C for 4 h. Next, the obtained g-C_3N_4 powder is achieved protonation by concentrated H_2SO_4 and ultrasonic stripping. Typically, 1 g of g-C_3N_4 powder was added into 20 mL H_2SO_4 (98 wt%), and the dispersion was stirred for 8 hours. Subsequently, the dispersion was slowly poured into 200 mL of deionized water and sonicated with 8 h for exfoliation. The products were then collected by centrifugation at 10000 rpm for 10 min, and washed several times with water. Finally, it was dried under vacuum at 50 °C.

2.3 Preparation of P-g-C_3N_4-WS_2 nanocomposite

P-g-C_3N_4-WS_2 nanocomposite were prepared by electrostatic self-assembly method with positively charged P-g-C_3N_4 nanosheets and negatively charged WS_2 nanosheets. In detail, different amount of P-g-C_3N_4 (25, 50, 100, 150, 200, 250 mg) was firstly added into 100 mL of 0.1 mM HCl solution, and then the dispersion was ultrasonicated for 2 h to form a milky white suspension. Then, 50 mg of WS_2 nanosheets was added into the suspension and it was then magnetically stirred for 6 h. Afterwards, the solution was centrifuged at 10000 rpm for 10 min. The sediment was collected and washed with deionized water for three times. Finally, it was freeze-dried under vacuum overnight. The obtained P-g-C_3N_4-WS_2 heterojuction was calcined at 300 °C for 2 h under N_2 flow to make the heterojunction structure stronger. To investigate the effect

of the ratio of P-g-C_3N_4 and WS_2 on the photoactivity, the P-g-C_3N_4-WS_2 composites prepared with different amounts of P-g-C_3N_4 were labeled as P-g-C_3N_4-WS_2-0.5, P-g-C_3N_4-WS_2-1, P-g-C_3N_4-WS_2-2, P-g-C_3N_4-WS_2-3, P-g-C_3N_4-WS_2-4 and P-g-C_3N_4-WS_2-5, where the ration for P-g-C_3N_4 and WS_2 were 1:05, 1:1, 1:2, 1:3, 1:4 and 1:5, respectively. In later experiment, we employed P-g-C_3N_4-WS_2-2 throughout the experiment due to the optimal photoactivity.

2.4 Synthesis of amino functionalized MnO_2 (MnO_2-NH_2) nanoflowers

MnO_2 nanoflowers were prepared based on the previous literature [31]. Briefly, 0.5 g $KMnO_4$ was dissolved in 250 mL deionized water and magnetically stirred for 30 min. Then, 5 mL oleic acid was slowly added into the $KMnO_4$ solution to reduce $KMnO_4$ to form a stable emulsion. After stirring at room temperature for 4 h, a brown-black product was collected with centrifugation and washed three times with water and ethanol, respectively. Finally, the product was dried 60 °C under vacuum.

MnO_2-NH_2 was synthesized using APTES as amination reagent. Firstly, MnO_2 nanoflowers (0.25 g), APTES (1 mL) and toluene (80 mL) were added into a two-necked round bottom flask. The mixture was stirred and refluxed for 6 h at 120 °C under N_2 atmosphere. Then, the product was collected with centrifugation, and washed three times with toluene and deionized water, respectively. Finally, it was dried in vacuum overnight.

2.5 Fabrication of the PEC biosensor and PEC detection

Before constructing the PEC sensing interface, the ITO conductive electrode is prepared. Briefly, ITO glass was firstly cut into sheet with the size of 1 × 5 cm. Then,

it was successively sonicated with acetone solution, ethanol/NaOH mixed solution (v/v = 1:1) and doubly distilled water for 15 min, respectively. After that, 40 μL of 2 mg/mL P-g-C_3N_4-WS_2-2 nanocomposite was carefully dropped on the bare ITO electrode, and dried under the irradiation of infrared lamp. The prepared electrode is named as C_3N_4-WS_2/ITO. Subsequently, 40 μL AuNPs dispersion was dropped onto the C_3N_4-WS_2/ITO electrode surface and dried under infrared lamp irradiation (the prepared electrode was denoted as AuNPs/C_3N_4-WS_2/ITO). Afterwards, 40 μL DNA probe immobilization buffer containing 1 μM probe DNA was dropped onto the AuNPs/C_3N_4-WS_2/ITO surface, and the electrode was incubated for 120 min in a humid environment at 37 °C. The prepared electrode was named as ssDNA/AuNPs/C_3N_4-WS_2/ITO. Then, the electrode surface was rinsed with washing buffer for 3 times to remove unreacted probe DNA. Next, the electrode was incubated with 40 μL of MCH for 30 min to block unreacted AuNPs. After rising with washing buffer for three times, 40 μL of DNA hybridization buffer containing 10 nM complementary DNA was dropped onto the electrode surface and incubated for 120 min in a humid cell at 37 °C. The fabricated electrode was noted as dsDNA-5fC/AuNPs/C_3N_4-WS_2/ITO. The electrode was then washed three times with washing buffer. Afterwards, 30 μL of 3 mg/mL of MnO_2-NH_2 was further dropped onto the above electrode surface, and incubated at room temperature for 120 min under humid environment. This electrode was labeled as MnO_2/dsDNA-5fC/AuNPs/C_3N_4-WS_2/ITO.

For PEC detection, MnO_2/dsDNA-5fC/AuNPs/C_3N_4-WS_2/ITO was employed as a working electrode, a Pt electrode was used as a counter electrode, a saturated calomel

electrode was used as a reference electrode. The PEC detection was performed on a CHI832A electrochemical workstation equipped with a 500 W xenon lamp as light source. To obtain visible light, an optical filter was employed. The applied potential is -0.4 V and the detection buffer is 10 mM Tris-HCl containing 10 mM AA solution (pH = 7.4).

3. Results and discussion

3.1 Detection strategy

In this work, P-g-C_3N_4-WS_2 heterojunction composite was firstly prepared by the electrostatic assembly of protonated g-C_3N_4 (P-g-C_3N_4) nanosheets and WS_2 nanosheeets, which was employed as photoactive material in the PEC biosensor fabrication. Amino functionalized MnO_2 nanoflowers was prepared and used as a signal quencher.

As shown in Scheme 1A, P-g-C_3N_4 nanosheets was firstly prepared using H_2SO_4 as exfoliation and protonation reagent, which also makes g-C_3N_4 possessing both amphoteric properties of carboxyl group and amino group. This amphoteric nature makes P-g-C_3N_4 positively charged under acidic conditions and negatively charged under alkaline conditions. WS_2 nanosheets were then prepared by the sonication-assisted liquid exfoliation of WS_2 powder in water containing poly(acrylic acid). After that, the self-assembly of P-g-C_3N_4 nanosheets and WS_2 nanosheets was performed based on the strong electrostatic attraction of positively charged g-C_3N_4 nanosheets (+17.9 mV) and negatively charged WS_2 nanosheets (-30.5 mV). More detailed, the P-g-C_3N_4 (-2.56 eV vs NHE) has a conductive edge potential lower than WS_2 (-0.26 eV

vs NHE) due to the proper energy level matching between the two materials. (The proof of P-g-C_3N_4-WS_2 heterojunction detection mechanism is illustrated in Fig 3). Therefore, electron on P-g-C_3N_4 nanosheets can be easily transferred to the CB of WS_2 nanosheets through interface contact, and then transferred to the surface of the ITO electrode to generate a stable photocurrent. At the same time, the introduction of P-g-C_3N_4 slows down the recombination rate of electron-hole pairs. Therefore, the nanocomposite photocurrent is higher than pure WS_2.

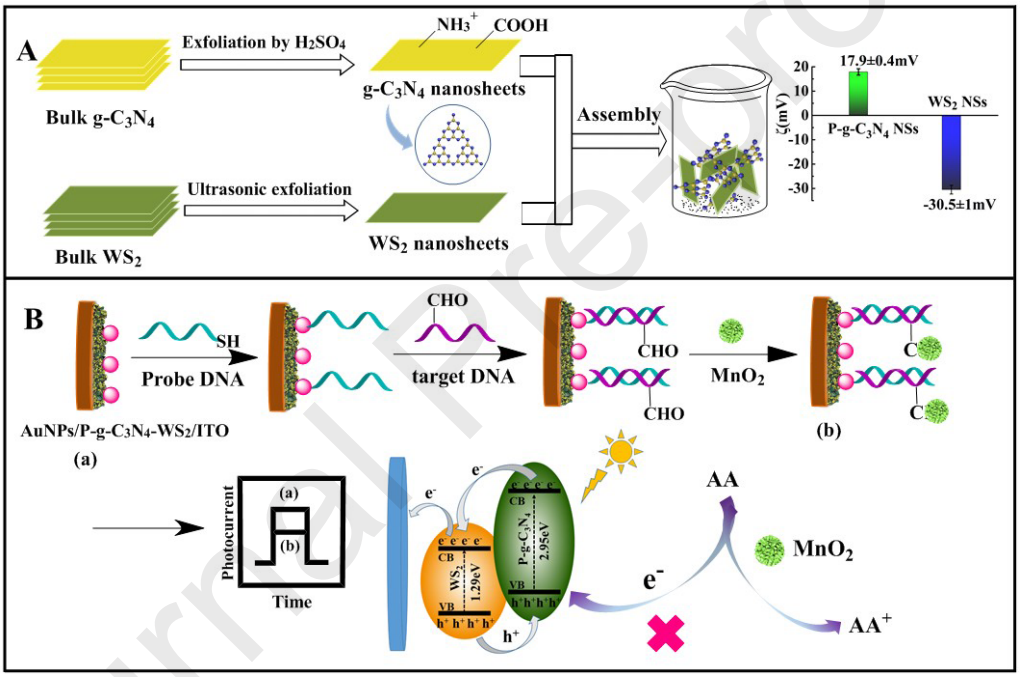

Scheme 1. Preparation principle of P-g-C_3N_4-WS_2 composite (A) and construction process of PEC biosensor (B).

The biosensors fabrication process and 5fC detection are shown in Scheme 1B. Firstly, P-g-C_3N_4-WS_2-2 nanocomposite was modified on ITO electrode surface, where P-g-C_3N_4-WS_2-2 nanocomposite was employed as photoactive material. Moreover, the P-g-C_3N_4-WS_2/ITO presented strong PEC response in the detection buffer (10 mM Tris-HCl containing 10 mM AA, pH = 7.4), where AA was used as electron donor to

provide electron and blocks the recombination of photogenerated electron and hole of photoactive material. Secondly, AuNPs were further modified on P-g-C_3N_4-WS_2/ITO surface. AuNPs have two functions. One is as probe DNA immobilization matrix using the formation of Au-S bond between AuNPs and the thiol group at the 3′-terminal of probe DNA. The other is as the accelerant for photogenerated electron, which can also improve the PEC response of the photoactive material. Then, probe DNA was assembled on AuNPs/P-g-C_3N_4-WS_2/ITO surface based on the formation of Au-S bond, and complementary DNA containing 5fC is further captured on electrode surface through the DNA hybridization event. Finally, the amino functionalized MnO_2 nanoflowers were captured on the electrode surface based on the specific covalent reaction between amino group and aldehyde group. Because MnO_2 nanoflowers could oxidize the electron donor of ascorbic acid in the detection buffer solution, the PEC response of the photoactive material decreased. Therefore, based on the relationship between the concentration of complementary DNA containing 5fC and the photocurrent, 5fC can be detected.

3.2 Characterization of nanomaterials

P-g-C_3N_4 nanosheets and WS_2 nanosheets were characterized by TEM and AFM. As shown in Fig. 1A and 1B, both P-g-C_3N_4 and WS_2 illustrates well layer structure. Fig. 1E and 1F present the AFM images of P-g-C_3N_4 nanosheets and WS_2 nanosheets. The thickness is about 2 nm and 3 nm for P-g-C_3N_4 nanosheet and WS_2 nanosheet, respectively. It is well known that single layer of P-g-C_3N_4 and WS_2 are 0.3 nm and 0.8 nm, which indicated that the layer number for P-g-C_3N_4 and WS_2 is 7 layers and 4 layers,

respectively [32, 33]. It powerfully demonstrates the successful exfoliation of P-g-C_3N_4 and WS_2.

Fig. 1C illustrates the TEM image of P-g-C_3N_4-WS_2-2 nanocomposite, which contains a number of irregular nanosheets. As shown in the inset HRTEM graph of Fig. 1C, the lattice spacing of the (100) crystal plane of WS_2 is 0.279 nm [34], and the amorphous region of the edge can prove the existence of P-g-C_3N_4 [35-37]. The P-g-C_3N_4-WS_2-2 nanocomposite was also characterized by XRD. As seen in Fig. 1D, all characteristic diffraction peaks are hexagonal-phase WS_2 (JCPDS card no. 85–1068) [34]. In addition, the peak at 27.1° is a typical diffraction peak of P-g-C_3N_4, which is related to the diffractive surface of (002), due to the inter-layer stacking of the graphite-like layer [38]. It can be seen from Fig. 1G that SEM demonstrates the successful combination of P-g-C_3N_4 and WS_2 nanosheets. In Fig. 1H, the elemental mapping indicates that the four elements (C, N, S and W) are evenly distributed. So it can be proved that these two substances are successfully coupled together. Moreover, it can be seen from of Fig. S2 that the broadband in the 3000-3500 cm^{-1} region of P-g-C_3N_4 is attributed to the stretching vibration of the primary amine group (-NH_2), and the WS_2 FT-IR spectrum further confirms the presence of PAA molecules [29]. After the combination of this two materials, since the -NH_2 in P-g-C_3N_4 reacts with -COOH in the WS_2 to form an amide bond, so the peak at 3000-3500 cm-1 is weakened. In addition, the P-g-C_3N_4-WS_2 composite has more stretching vibration peaks of the triazine ring, and the peaks at 1572 and 1632 cm^{-1} can be attributed to C = N stretching vibration. The three peaks at 1253, 1320 and 1425 cm^{-1} correspond to the aromatic C-N stretching

mode. The peak at 807 cm^{-1} is the triazine ring breathing pattern [39]. According to the above characterization, P-g-C_3N_4-WS_2 nanocomposite was successful prepared.

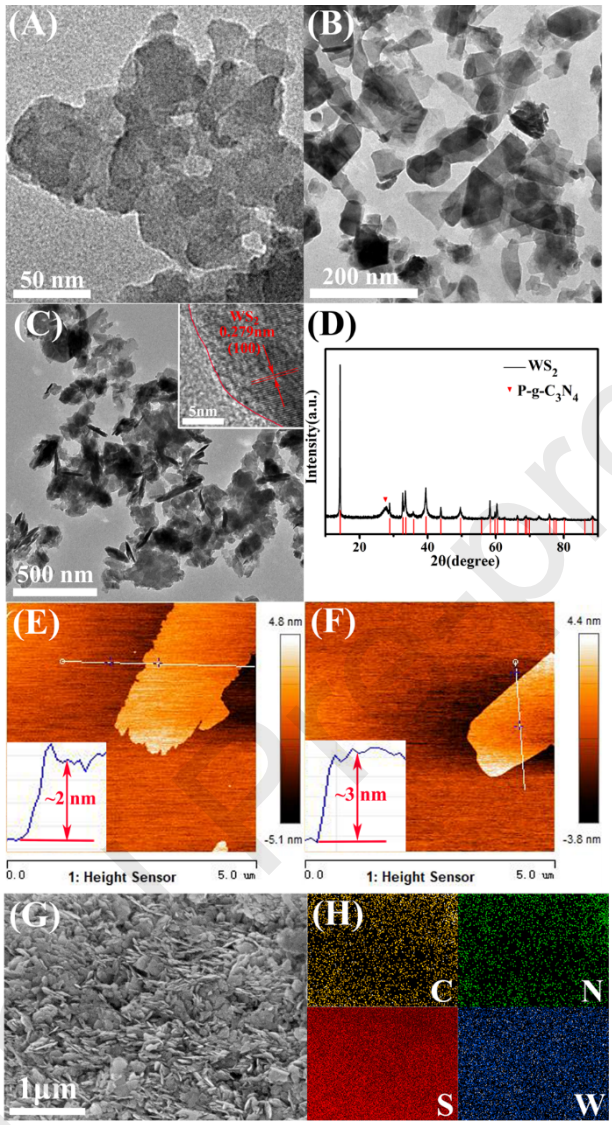

Fig. 1. TEM images of P-g-C_3N_4 nanosheets (A) and WS_2 nanosheets (B). (C) TEM and HRTEM image of P-g-C_3N_4-WS_2-2 nanocomposite. (D) XRD image of P-g-C_3N_4-WS_2-2 nanocomposite. AFM image of P-g-C_3N_4 nanosheets (E) and WS_2 nanosheets (F). SEM image (G) and corresponding EDS elemental maps (H) for P-g-C_3N_4-WS_2-2 nanocomposite.

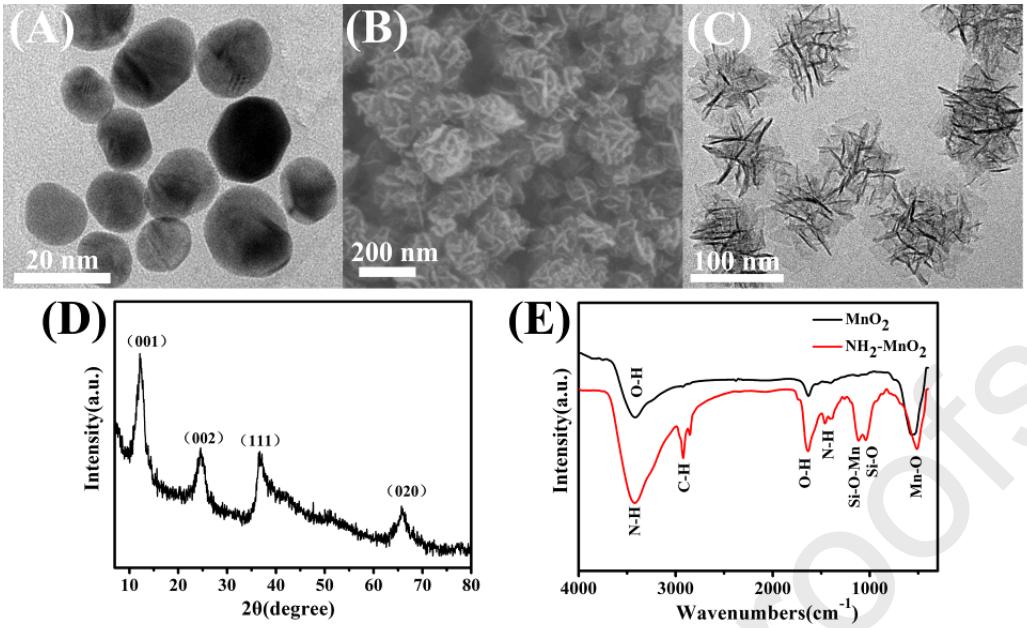

Fig. 2. (A) TEM image of AuNPs. (B-D) SEM, TEM, and XRD pattern of MnO_2-NH_2, respectively. (E) FT-IR spectra of MnO_2 and MnO_2-NH_2.

Fig. 2A shows the TEM image of AuNPs, which indicates that AuNPs are approximately spherical structure with the average diameter at around 20 nm. Furthermore, MnO_2-NH_2 were also characterized. As shown in Fig. 2B and 2C, MnO_2-NH_2 is nanoflower structure containing many nanoflake. The diameter for these nanoflower is about 100 nm. The XRD pattern of the MnO_2-NH_2 confirms the monoclinic layered structure (JCPDS42-1317) (Fig. 2D). The three broad peaks at around 12°, 37° and 66° can be directed to the birnessite-type MnO_2 [31, 40-42], demonstrating the successful preparation of manganese dioxide. The FT-IR spectra of MnO_2-NH_2 shows that tensile or bending vibration at 1049, 1097, 1367, and 1576 cm^{-1} are assigned to (Si-O)n, Si-OMn, C-N and N-H [31] (Fig. 2E). It proves that the surface of the MnO_2 nanoflower was successfully modified with amino groups.

The PEC response of P-g-C_3N_4, WS_2, P-g-C_3N_4-WS_2-2 was investigated and compared. As seen in Fig. 3A, the photocurrent for P-g-C_3N_4, WS_2 and P-g-C_3N_4-WS_2-2 are 187, 305 and 1256 nA, respectively. The strong photocurrent for P-g-C_3N_4-WS_2-2 may be attributed to the formation of heterojunction structure of P-g-C_3N_4 and WS_2. To prove it, the energy band structure of P-g-C_3N_4 and WS_2 were investigated in detail using Mott-Schottky, VB-XPS and UV-vis diffuse reflectance spectrum. It can be seen from Fig. 3B and Fig. 3E that the slopes of WS_2 and P-g-C_3N_4 are positive, which demonstrates that WS_2 and P-g-C_3N_4 are n-type semiconductor. Compared with saturated calomel electrodes (SCE), the flat potentials are -0.32 V and -2.45 V for WS_2 and P-g-C_3N_4, respectively [43]. Compared to the conventional hydrogen electrode (NHE), their values are -0.12 V and -2.25 V, respectively. Since the Fermi level is approximately equal to the flat band potential, so the Fermi levels of WS_2 and P-g-C_3N_4 are -0.12 V and -2.25 V, respectively. As can be seen from the VB-XPS shown in Fig. 3C and 3F, the energy gap between the valence band and the Fermi level (E_f) of WS_2 and P-g-C_3N_4 are 1.15 eV and 2.64 eV [34, 38], respectively. Therefore, the VB potentials (E_{vb}) of WS_2 and P-g-C_3N_4 are estimated to be 1.03 eV and 0.39 eV, respectively. According to UV-vis diffuse reflectance spectra (Fig. 3D and 3G), we can obtain the band gap energy (E_g), so the conduction band potentials (E_{cb}) of WS_2 and P-g-C_3N_4 were calculated to be -0.26 eV and -2.56 eV, respectively ($E_{vb} = E_{cb} + E_g$) [44]. From the above test results, we calculated the energy band structure diagram of WS_2 and P-g-C_3N_4 nanosheets (Fig. 3H). In general, the transfer of photogenerated electrons and holes between the two semiconductors is considered to be a heterostructure

mechanism due to the energy level matching of P-g-C_3N_4 and WS_2.

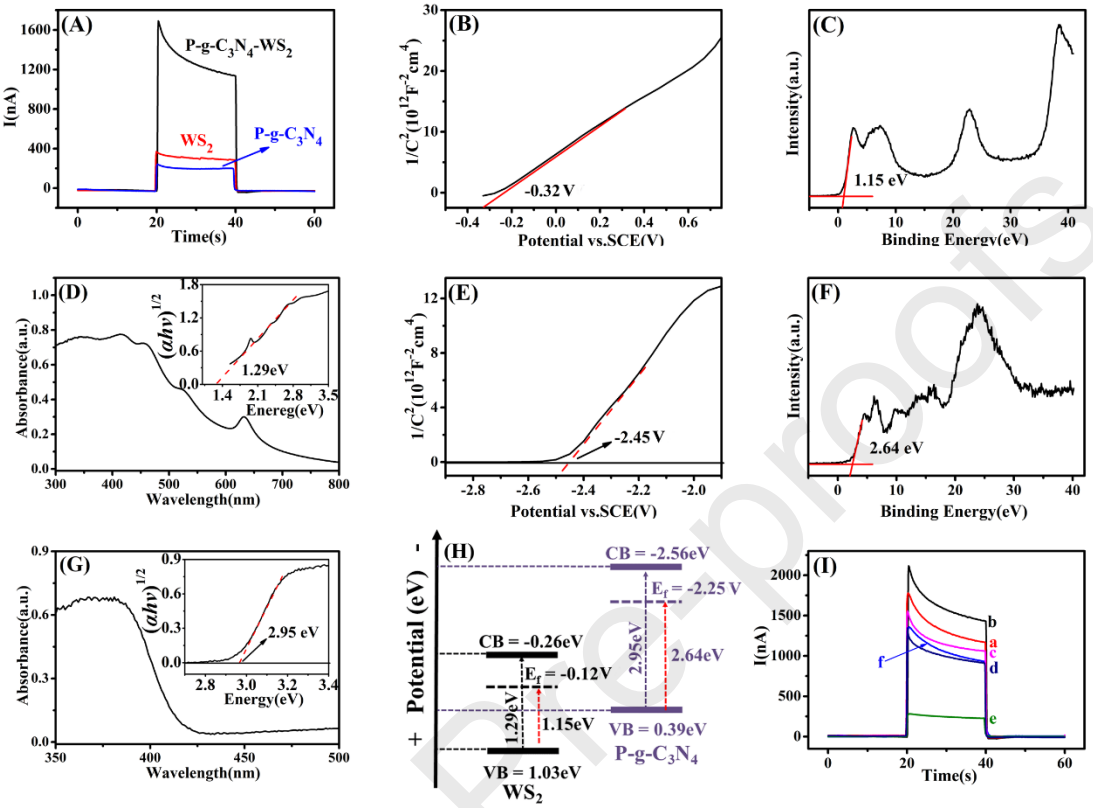

Fig. 3. (A) The photocurrent responses of P-g-C_3N_4/ITO, WS_2/ITO, P-g-C_3N_4-WS_2/ITO in 10 mM Tris-HCl containing 10 mM AA (pH 7.4). (B) Mott-Schottky plots of WS_2. (C) VB-XPS spectra of WS_2. (D) UV-vis diffuse reflectance spectra of WS_2. (E) Mott-Schottky plots of P-g-C_3N_4. (F) VB-XPS spectra of P-g-C_3N_4. (G) UV-vis diffuse reflectance spectra of P-g-C_3N_4. (H) Schematic band structure of WS_2 and P-g-C_3N_4. (I) PEC response of different electrodes in 10 mM Tris-HCl containing 10 mM AA solution (pH = 7.4). (a) C_3N_4-WS_2/ITO, (b) AuNPs/C_3N_4-WS_2/ITO, (c) ssDNA/AuNPs/C_3N_4-WS_2/ITO, (d) dsDNA-5fC/AuNPs/C_3N_4-WS_2/ITO, (e) MnO_2/dsDNA-5fC/AuNPs/C_3N_4-WS_2/ITO, (f) ssDNA/AuNPs/C_3N_4-WS_2/ITO after incubation with MnO_2. Applied potential is -0.4 V. 5fC-DNA concentration is 10 nM.

As shown in Figures 3A-H, the photocurrent intensity of the P-g-C_3N_4-WS_2-2 heterojunction was significantly higher than that of the pure P-g-C_3N_4 and pure WS_2 nanosheets, indicating that the separation and migration of photoelectrons and holes were enhanced after the combination of P-g-C_3N_4 and WS_2 materials. This significant improvement is mainly due to the accelerated charge separation and migration rate, which is due to the formation of heterojunction between the two components. As far as we know, both P-g-C_3N_4 and WS_2 can be excited and produce electron-hole pairs under visible light illumination. The E_{CB} of P-g-C_3N_4 (-2.56 eV) is more negative than WS_2 (-0.26 eV), so the excited electrons in P-g-C_3N_4 can be directly injected into the CB of WS_2. At the same time, since the VB position of P-g-C_3N_4 is much lower than the VB position of WS_2, the photogenerated holes in WS_2 are easily transferred to the VB of P-g-C_3N_4. Therefore, we demonstrate the successful formation of P-g-C_3N_4-WS_2-2 heterostructures and the mechanism of photocurrent enhancement.

3.3 Characterization of the modified electrodes

In order to verify the detection feasibility of PEC biosensor for 5fC-DNA detection, the photocurrent responses of different electrodes were tested in 10 mM Tris-HCl containing 10 mM AA (pH 7.4). As shown in Fig. 3I, curve a is the photocurrent of C_3N_4-WS_2/ITO electrode under visible light irradiation. According to the result obtained at Fig. 3A-H, this strong photocurrent can be ascribed to the heterojunction structure of WS_2 nanosheets and P-g-C_3N_4 nanosheets, which reduces the

recombination rate of electron-hole pair and accelerates interface electron transfer to produce a stable initial photocurrent [45]. After the modification of AuNPs, the photocurrent increases greatly (curve b), which can be ascribed to the increased electrode surface area and the improved interface electron transfer rate causing by AuNPs. However, the photocurrent decreases when probe DNA (curve c) and 5-fC DNA (curve d) are successively modified on the electrode surface. It can be attributed to the electrostatic repulsion effect and steric hindrance effect of the DNA, which blocks the transfer of electron donor of AA to electrode surface and increases the recombination of photogenerated electron and hole. Thus, the photocurrent decreases. After the MnO_2-NH_2 was modified on the electrode surface, the photocurrent further decreases (curve e). The MnO_2 nanoflowers can oxidize the ascorbic acid [46], which can cause the decrease of AA concentration in detection buffer. As a result, the recombination of photogenerated electron and hole of the photoactive material improved, causing thedecrease the photocurrent. To further prove the detection possibility of this method, another control experiment was performed. The ssDNA/C_3N_4-WS_2/ITO electrode was directly incubated with MnO_2-NH_2 for 120 min, then the photocurrent was recorded. As shown in Fig. 3I, curve f, the PEC response is similar with ssDNA/P-g-C_3N_4-WS_2/ITO and higher than that obtained at MnO_2/5fC-dsDNA/P-g-C_3N_4-WS_2/ITO electrode. The results show that MnO_2-NH_2 cannot be successfully modified onto the electrode without complementary 5fC-DNA. Therefore, the biosensor can be used for 5fC detection.

EIS measurements were used to characterize the interface properties of the

prepared different electrodes. As shown in Fig. S3, the bare ITO electrode presented a semi-circle structure in high frequency region, indicating an interface electron transfer resistance (R_{et}) of 201 Ω (curve a). After the modification of P-g-C_3N_4-WS_2-2, the diameter of the semi-circle in high frequency region decreased (curve b), indicating the reduced interface electron transfer resistance. The Zeta potential of P-g-C_3N_4-WS_2-2 is 3 mV (Fig. S1), which proves the electropositivity of the composite. Thus, P-g-C_3N_4-WS_2-2 can facilitate the diffusion of the electronegative electron donor of AA to electrode surface due to the electrostatic adsorption effect. The interface electron transfer resistance further decreased when AuNPs were modified on the electrode surface (curve c), which could be attributed to the good conductivity of AuNPs. After accessing the probe DNA and complementary DNA (containing 5fC base), the interface electron transfer resistance gradually increased (curve d and e), which could be ascribed to the steric hindrance effect and electrostatic repulsion effect of DNA. When MnO_2 was immobilized on the electrode surface, the interface electron transfer resistance further increased (curve f), causing by the weak conductivity of MnO_2. Base on the change of the interface electron transfer resistance, the successful preparation of the modified electrodes can be confirmed.

In addition, the SEM image of different electrodes were also measured and the results were illustrated in Fig. S4 in Supplementary Material.

3.4 Optimization experimental conditions of biosensor

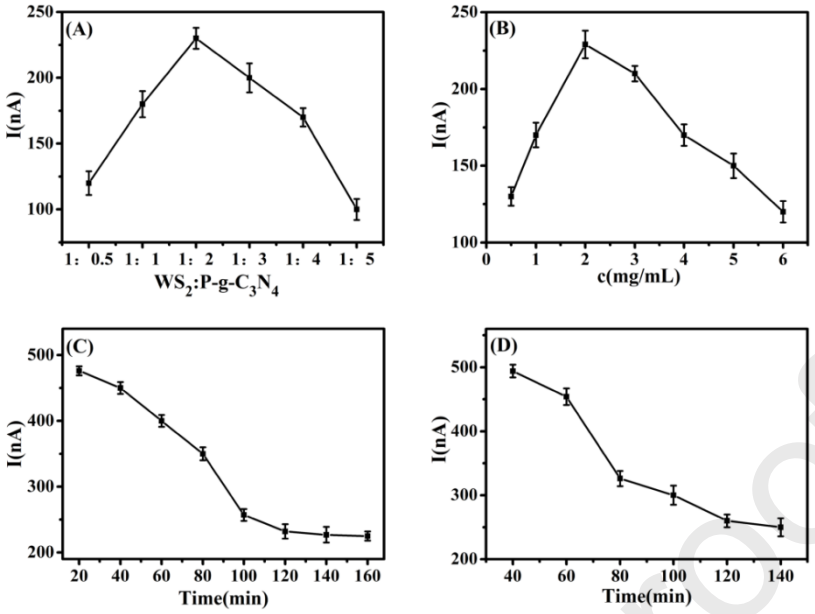

Fig. 4. Effect of proportions of WS_2 and P-g-C_3N_4 (A), P-g-C_3N_4-WS_2 concentration (B), DNA hybridization time (C) and MnO_2-NH_2 immobilization time (D) on the PEC response.

In order to improve the sensitivity and accuracy of biosensors, various experimental conditions have been optimized, including proportions of WS_2 and P-g-C_3N_4, P-g-C_3N_4-WS_2-2 concentration, DNA hybridization time, MnO_2-NH_2 immobilization time and the applied potential, pH values, the concentration of electron donor.

Fig. 4A shows the effect of different ratios of WS_2 and P-g-C_3N_4 on the PEC response. With changing the proportion of WS_2 and P-g-C_3N_4 from 1:0.5 to 1:5, the photocurrent firstly increases greatly, and then the photocurrent decreases gradually. The maximum photocurrent was achieved with the proportion of 1:2. Thus this proportion was employed.

Fig. 4B shows the effect of P-g-C_3N_4-WS_2-2 concentrations on the PEC response. The photocurrent increases with increasing P-g-C_3N_4-WS_2-2 concentration from 0.5 to 2.0 mg/mL. Then, the photocurrent decreases when further increasing P-g-C_3N_4-WS_2-2 concentration, which might be attributed to the increased thickness of P-g-C_3N_4-WS_2-2, blocking the transfer of the photogenerated electron and increasing the recombination of photogenerated electron and hole. Therefore, 2 mg/mL P-g-C_3N_4-WS_2-2 was selected for the subsequent experiments.

Fig. 4C is the effect of DNA hybridization time on the PEC response. When extending the hybridization time from 20 to 120 min, the photocurrent decreases gradually. However, the photocurrent tends to level off when further prolonging the hybridization time, which might be ascribed the approximately saturated hybridization of DNA. Therefore, 120 min was used in this work.

Fig. 4D shows the effect of MnO_2-NH_2 immobilization time on the PEC response. With increasing the immobilization time to 120 min, the photocurrent decreases gradually. And the photocurrent tends to level off when further prolonging the immobilization time. Thus, 120 min was used in this work.

Except the above experimental conditions, three other parameters (the applied potential, pH values and the concentration of electron donor) were also optimized and the results were listed in Supplementary Material (Fig. S5). The optimal results were -0.4 V, 7.4 and 10 mM for the applied potential, pH values and the concentration of electron donor, respectively.

3.5 Detection performance

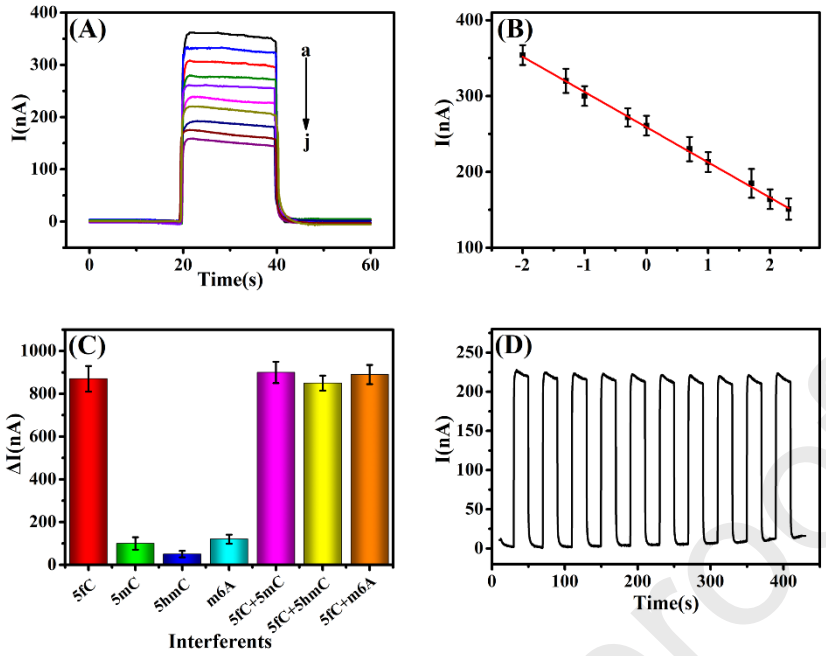

Fig. 5. (A) The PEC response of the biosensor with different concentrations of 5fC-DNA in 10 mM Tris-HCl containing 10 mM AA (pH 7.4). a-j: 0.01, 0.05, 0.1, 0.5, 1, 5, 10, 50, 100, 200 nM. (B) Linear relationship between the photocurrent and the logarithm value of 5fC-DNA concentration. (C) The histogram of photocurrent change for the biosensor fabricated with different targets. (D) Time–based photocurrent response of the biosensor in 10 mM Tris-HCl containing 10 mM AA (pH = 7.4) with light on and off cycles.

In order to investigate the detection sensitivity of the biosensor for 5fC-DNA, the PEC response of the biosensor with different concentrations of 5fC-DNA was recorded under the optimal experimental conditions. As shown in Fig. 5A, the photocurrent decreases with changing 5fC-DNA concentration from 0.01 – 200 nM. The photocurrent shows a linear relationship with the logarithm value of 5fC-DNA concentration (Fig. 5B). The linear regression equation is I (nA) = -46.41log$c$ (nM) +

258.97 with the linear correlation coefficient of 0.9990. The detection limit is estimated to be 3.8 pM (S/N = 3). The detection range and detection limit of this work is be superior to fluorescence method [47-49]. Though the detection limit for PEC biosensor is higher than that obtained at mass spectrometry-base technique [2, 50], the detection superiority of this work is also evident, such as simple operation, inexpensive instrument, low dosage for target molecule, fast signal response, etc.

Table 1. Performance comparison of the PEC biosensor for 5fC detection with other methods.

Methods	Linear range	Detection limit	Reference
Fluorescence	50-1000 nM	42 nM	[47]
Fluorescence	20-200 pM	20 pM	[48]
Fluorescence	50-200 nM	10 nM	[49]
LC-ESI-MS/MS	0.5-100 fM	0.11 fM	[51]
Mass spectrometry	0.1-100 fM	0.03 fM	[2]
Photoelectrochemistry	0.01-200 nM	3.8 pM	This work

Detection selectivity is an important performance for biosensor, thus it was investigated using 5mC-DNA, 5hmC-DNA, and 5mC-RNA as possible interferents. To perform it, the MnO_2/dsDNA-5fC/AuNPs/C_3N_4-WS_2/ITO was fabricated as described in section 2.5 except that 5fC-DNA was replaced by other interferent DNA. Then, the photocurrent change ($\Delta I = I_2 - I_1$) was compared, where I_1 is the photocurrent of

ssDNA/AuNPs/C_3N_4-WS_2/ITO, and I_2 is the photocurrent of ssDNA/AuNPs/C_3N_4-WS_2/ITO incubated with different DNA (5fC-DNA, 5mC-DNA, 5hmC-DNA, and 5mC-RNA) and MnO_2-NH_2 successively. As shown in Fig. 5C, the ΔI for the biosensor fabricated with 5fC-DNA is greatly higher than that obtained at the biosensor with other DNA, indicating that the developed method has high detection selectivity for 5fC-DNA. To further prove the detection specificity, the electrode was prepared with the mixture of 5fC-DNA and other three interferent DNA, respectively. The photocurrent for 5fC-DNA was similar with the mixture of 5fC-DNA and other interferent DNA. These results further prove the high detection specificity of the developed method.

Stability is also an important detection performance for biosensor, thus it was also evaluated. As illustrated in Fig. 5D, the photocurrent of MnO_2/5fC-dsDNA/AuNPs/C_3N_4-WS_2/ITO in detection buffer was recorded over a number of light on and off cycles. The result indicates that no significant change in the photocurrent response is observed (the RSD is 1.16%), which demonstrates the good detection stability of the developed method.

The detection reproducibility was also assessed by comparing the photocurrent of seven MnO_2/dsDNA-5fC/AuNPs/C_3N_4-WS_2/ITO electrodes, where the electrodes were fabricated with the same process ass described in section 2.5. As illustrated in Fig. S6, the RSD is 3.12% for the photocurrent of the seven biosensors, which indicates the acceptable detection reproducibility.

4. Conclusions

In summary, a novel PEC biosensor was fabricated for 5fC detection using the aldehyde

covalent reaction for 5fC recognition and capture. Due to the heterogeneous structure, the PEC activity of P-g-C_3N_4-WS_2 nanocomposite was improved greatly, which can largely increase the detection sensitivity. Due to the DNA hybridization and the specific covalent reaction of the aldehyde group in 5fC, 5fC can be specific recognized and captured on the substrate electrode surface. Finally, utilizing the oxidation ability of MnO_2 nanoflowers towards the electron donor of AA in the detection buffer, the PEC signal of the photoactive material decreases greatly, which achieves the successful detection of 5fC. More importantly, this method has the advantages of simple operation, inexpensive instrument, high specificity and low detection limit.

Acknowledgements

This work is supported by the Natural Science Foundation of Shandong Province of China (No. ZR2018MB028), Key research and development project of Shandong Province (No. 2019GSF107023), and the National Natural Science Foundation of China (Nos. 21775090, 41807484, 41977345).

References

[1] Y. Wang, X. Zhang, G. Zou, S. Peng, C. Liu, X. Zhou, Detection and application of 5-formylcytosine and 5-formyluracil in DNA, Accounts. Chem. Res. 52(4) (2019) 1016-1024.

[2] H.-P. Jiang, T. Liu, N. Guo, L. Yu, B.-F. Yuan, Y.-Q. Feng, Determination of formylated DNA and RNA by chemical labeling combined with mass spectrometry analysis, Anal. Chim. Acta 981 (2017) 1-10.

[3] C. Liu, Y. Wang, W. Yang, F. Wu, W. Zeng, Z. Chen, J. Huang, G. Zou, X. Zhang,

S. Wang, X. Weng, Z. Wu, Y. Zhou, X. Zhou, Fluorogenic labeling and single-base resolution analysis of 5-formylcytosine in DNA, Chem. Sci. 8(11) (2017) 7443-7447.

[4] W.-W. Zhao, J.-J. Xu, H.-Y. Chen, Photoelectrochemical enzymatic biosensors, Biosens. Bioelectron. 92 (2017) 294-304.

[5] W. Jiang, L. Wu, J. Duan, H. Yin, S. Ai, Ultrasensitive electrochemiluminescence immunosensor for 5-hydroxymethylcytosine detection based on Fe_3O_4@SiO_2 nanoparticles and PAMAM dendrimers, Biosens. Bioelectron. 99 (2018) 660-666.

[6] B. Li, Y. Chen, A. Peng, X. Chen, X. Chen, Improved photoelectrochemical properties of tungsten oxide by modification with plasmonic gold nanoparticles for the non-enzymatic sensing of ethanol, J. Colloid Interf. Sci 537 (2019) 528-535.

[7] H. Shang, H. Xu, L. Jin, C. Chen, T. Song, C. Wang, Y. Du, Electrochemical-photoelectrochemical dual-mode sensing platform based on advanced Cu_9S_8/polypyrrole/ZIF-67 heterojunction nanohybrid for the robust and selective detection of hydrogen sulfide, Sensor. Actuat. B-Chem. 301 (2019) 127060.

[8] Y. Zang, J. Lei, H. Ju, Principles and applications of photoelectrochemical sensing strategies based on biofunctionalized nanostructures, Biosens. Bioelectron. 96 (2017) 8-16.

[9] Y. Wang, H. Yin, X. Li, G.I.N. Waterhouse, S. Ai, Photoelectrochemical immunosensor for N6-methyladenine detection based on Ru@UiO-66, Bi_2O_3 and Black TiO_2, Biosens. Bioelectron. 131 (2019) 163-170.

[10] L.-B. Zhu, L. Lu, H.-Y. Wang, G.-C. Fan, Y. Chen, J.-D. Zhang, W.-W. Zhao, Enhanced organic−inorganic heterojunction of polypyrrole@Bi_2WO_6: Fabrication and

application for sensitive photoelectrochemical immunoassay of creatine kinase-MB, Biosens. Bioelectron. 140 (2019) 111349.

[11] X. Li, L. Zhu, Y. Zhou, H. Yin, S. Ai, Enhanced photoelectrochemical method for sensitive detection of protein kinase A activity using TiO_2/g-C_3N_4, PAMAM dendrimer, and alkaline phosphatase, Anal. Chem. 89(4) (2017) 2369-2376.

[12] M. Wang, H. Yin, Y. Zhou, X. Meng, G.I.N. Waterhouse, S. Ai, A novel photoelectrochemical biosensor for the sensitive detection of dual microRNAs using molybdenum carbide nanotubes as nanocarriers and energy transfer between CQDs and AuNPs, Chem. Eng. J. 365 (2019) 351-357.

[13] Q. Zhou, H. Xue, Y. Zhang, Y. Lv, H. Li, S. Liu, Y. Shen, Y. Zhang, Metal-free all-carbon nanohybrid for ultrasensitive photoelectrochemical immunosensing of alpha-fetoprotein, ACS Sensors 3(7) (2018) 1385-1391.

[14] J.-T. Cao, B. Wang, Y.-X. Dong, Q. Wang, S.-W. Ren, Y.-M. Liu, W.-W. Zhao, Photogenerated hole-Induced chemical redox cycling on Bi_2S_3/$Bi_2Sn_2O_7$ heterojunction: Toward general amplified split-type photoelectrochemical immunoassay, ACS Sensors 3(6) (2018) 1087-1092.

[15] R. Atchudan, N. Muthuchamy, T.N.J.I. Edison, S. Perumal, R. Vinodh, K.H. Park, Y.R. Lee, An ultrasensitive photoelectrochemical biosensor for glucose based on bio-derived nitrogen-doped carbon sheets wrapped titanium dioxide nanoparticles, Biosens. Bioelectron. 126 (2019) 160-169.

[16] B. Çakıroğlu, M. Özacar, A self-powered photoelectrochemical biosensor for H_2O_2, and xanthine oxidase activity based on enhanced chemiluminescence resonance energy

transfer through slow light effect in inverse opal TiO_2, Biosens. Bioelectron. 141 (2019) 111385.

[17] J. Shen, J. Wu, M. Wang, P. Dong, J. Xu, X. Li, X. Zhang, J. Yuan, X. Wang, M. Ye, R. Vajtai, J. Lou, P.M. Ajayan, Surface tension components based selection of cosolvents for efficient liquid phase exfoliation of 2D materials, Small 12(20) (2016) 2741-2749.

[18] X. Li, Y. Li, Q. Qiu, Q. Wen, Q. Zhang, W. Yang, L. Yuwen, L. Weng, L. Wang, Efficient biofunctionalization of MoS_2 nanosheets with peptides as intracellular fluorescent biosensor for sensitive detection of caspase-3 activity, J. Colloid Interf. Sci 543 (2019) 96-105.

[19] J. Wang, K. Zhang, H. Xu, B. Yan, F. Gao, Y. Shi, Y. Du, Engineered photoelectrochemical platform for the ultrasensitive detection of caffeic acid based on flower-like MoS_2 and PANI nanotubes nanohybrid, Sensor. Actuat. B-Chem. 276 (2018) 322-330.

[20] C. Sui, T. Wang, Y. Zhou, H. Yin, X. Meng, S. Zhang, G.I.N. Waterhouse, Q. Xu, Y. Zhuge, S. Ai, Photoelectrochemical biosensor for hydroxymethylated DNA detection and T4-β-glucosyltransferase activity assay based on WS_2 nanosheets and carbon dots, Biosens. Bioelectron. 127 (2019) 38-44.

[21] S. Luo, S. Dong, C. Lu, C. Yu, Y. Ou, L. Luo, J. Sun, J. Sun, Rational and green synthesis of novel two-dimensional WS_2/MoS_2 heterojunction via direct exfoliation in ethanol-water targeting advanced visible-light-responsive photocatalytic performance, J. Colloid Interf. Sci 513 (2018) 389-399.

[22] Y. Pi, B. Liu, Z. Li, Y. Zhu, Y. Li, F. Zhang, G. Zhang, W. Peng, X. Fan, TiO_2 nanorod arrays decorated with exfoliated WS_2 nanosheets for enhanced photoelectrochemical water oxidation, J. Colloid Interf. Sci 545 (2019) 282-288.

[23] J. Wang, B. Yang, S. Li, B. Yan, H. Xu, K. Zhang, Y. Shi, C. Zhai, Y. Du, Enhanced photo-electrochemical response of reduced graphene oxide and C_3N_4 nanosheets for rutin detection, J. Colloid Interf. Sci 506 (2017) 329-337.

[24] Y. Zou, J.-W. Shi, D. Ma, Z. Fan, L. Cheng, D. Sun, Z. Wang, C. Niu, WS_2/graphitic carbon nitride heterojunction nanosheets decorated with CdS quantum dots for photocatalytic hydrogen production, ChemSusChem 11(7) (2018) 1187-1197.

[25] J. Huang, J. Mei, J. Han, H. Liang, W. Wang, B. Dong, L. Cao, Vertical 1T/2H-WS_2 nanoflakes grown on 2D-C_3N_4: Multiple charge transfer channels designed for enhanced photocatalytic activity, J. Colloid Interf. Sci 556 (2019) 224-231.

[26] R. Deng, X. Xie, M. Vendrell, Y.-T. Chang, X. Liu, Intracellular glutathione detection using MnO_2-nanosheet-modified upconversion nanoparticles, J. Am. Chem. Soc. 133(50) (2011) 20168-20171.

[27] J. Dietzsch, D. Feineis, C. Höbartner, Chemoselective labeling and site-specific mapping of 5-formylcytosine as a cellular nucleic acid modification, Febs. Lett. 592(12) (2018) 2032-2047.

[28] J. Hu, X. Xing, X. Xu, F. Wu, P. Guo, S. Yan, Z. Xu, J. Xu, X. Weng, X. Zhou, Selective chemical labelling of 5-formylcytosine in DNA by fluorescent dyes, Chem.–Eur. J. 19(19) (2013) 5836-5840.

[29] Y. Yuan, R. Li, Z. Liu, Establishing water-soluble layered WS_2 nanosheet as a

platform for biosensing, Anal. Chem. 86(7) (2014) 3610-3615.

[30] F. Cheng, H. Wang, X. Dong, The amphoteric properties of g-C_3N_4 nanosheets and fabrication of their relevant heterostructure photocatalysts by an electrostatic re-assembly route, Chem. Commun. 51(33) (2015) 7176-7179.

[31] Y. Zhang, M. Su, L. Ge, S. Ge, J. Yu, X. Song, Synthesis and characterization of graphene nanosheets attached to spiky MnO_2 nanospheres and its application in ultrasensitive immunoassay, Carbon 57 (2013) 22-33.

[32] Y. Wang, L. Li, Y. Wei, J. Xue, H. Chen, L. Ding, J. Caro, H. Wang, Water transport with ultralow friction through partially exfoliated g-C_3N_4 nanosheet membranes with self-supporting spacers, Angew. Chem. Int. Edit. 56(31) (2017) 8974-8980.

[33] Z.-Q. Xu, Y. Zhang, S. Lin, C. Zheng, Y.L. Zhong, X. Xia, Z. Li, P.J. Sophia, M.S. Fuhrer, Y.-B. Cheng, Q. Bao, Synthesis and transfer of large-area monolayer WS_2 crystals: Moving toward the recyclable use of sapphire substrates, ACS Nano 9(6) (2015) 6178-6187.

[34] Y. Sang, Z. Zhao, M. Zhao, P. Hao, Y. Leng, H. Liu, From UV to near-infrared, WS_2 Nanosheet: a novel photocatalyst for full solar light spectrum photodegradation, Adv Mater 27(2) (2015) 363-369.

[35] J. Li, E. Liu, Y. Ma, X. Hu, J. Wan, L. Sun, J. Fan, Synthesis of MoS_2/g-C_3N_4 nanosheets as 2D heterojunction photocatalysts with enhanced visible light activity, Appl. Surf. Sci. 364 (2016) 694-702.

[36] H. Li, J. Liu, W. Hou, N. Du, R. Zhang, X. Tao, Synthesis and characterization of

g-C_3N_4/Bi_2MoO_6 heterojunctions with enhanced visible light photocatalytic activity, Appl. Catal. B-Environ. 160-161 (2014) 89-97.

[37] Y. Hong, C. Li, G. Zhang, Y. Meng, B. Yin, Y. Zhao, W. Shi, Efficient and stable Nb_2O_5 modified g-C_3N_4 photocatalyst for removal of antibiotic pollutant, Chem. Eng. J. 299 (2016) 74-84.

[38] K. Li, X. Xie, W.-D. Zhang, Photocatalysts based on g-C_3N_4-encapsulating carbon spheres with high visible light activity for photocatalytic hydrogen evolution, Carbon 110 (2016) 356-366.

[39] M.S. Akple, J. Low, S. Wageh, A.A. Al-Ghamdi, J. Yu, J. Zhang, Enhanced visible light photocatalytic H_2-production of g-C_3N_4/WS_2 composite heterostructures, Appl. Surf. Sci. 358 (2015) 196-203.

[40] J. Yan, Z. Fan, T. Wei, W. Qian, M. Zhang, F. Wei, Fast and reversible surface redox reaction of graphene–MnO_2 composites as supercapacitor electrodes, Carbon 48(13) (2010) 3825-3833.

[41] Q.Y. Shan, X.L. Guo, F. Dong, Y.X. Zhang, Single atom (K/Na) doped graphitic carbon Nitride@MnO_2 as an efficient electrode Material for supercapacitor, Mater. Lett. 202 (2017) 103-106.

[42] N. Yu, H. Yin, W. Zhang, Y. Liu, Z. Tang, M.-Q. Zhu, High-performance fiber-shaped all-solid-state asymmetric supercapacitors based on ultrathin MnO_2 nanosheet/carbon fiber cathodes for wearable electronics, Adv. Energy Mater. 6(2) (2016) 1501458.

[43] H.-B. Fang, N. Li, Z. Xue, Y. Zhang, Y.-Z. Zheng, X. Tao, Efficient charge

separation promoting visible-light-driven photocatalytic activity of MnO_x decorated WS_2 hybrid nanosheets, Electrochem. Commun. 72 (2016) 118-121.

[44] H. Huang, R. Cao, S. Yu, K. Xu, W. Hao, Y. Wang, F. Dong, T. Zhang, Y. Zhang, Single-unit-cell layer established Bi_2WO_6 3D hierarchical architectures: Efficient adsorption, photocatalysis and dye-sensitized photoelectrochemical performance, Appl. Catal. B-Environ. 219 (2017) 526-537.

[45] R. Kumar, D. Das, A.K. Singh, C_2N/WS_2 van der Waals type-II heterostructure as a promising water splitting photocatalyst, J. Catal. 359 (2018) 143-150.

[46] W. Zhai, C. Wang, P. Yu, Y. Wang, L. Mao, Single-layer MnO_2 nanosheets suppressed fluorescence of 7-hydroxycoumarin: Mechanistic study and application for sensitive sensing of ascorbic acid in vivo, Anal. Chem. 86(24) (2014) 12206-12213.

[47] P. Guo, S. Yan, J. Hu, X. Xing, C. Wang, X. Xu, X. Qiu, W. Ma, C. Lu, X. Weng, X. Zhou, Selective detection of 5-formyl-2′-deoxycytidine in DNA using a fluorogenic hydroxylamine reagent, Org. Lett. 15(13) (2013) 3266-3269.

[48] Y. Wang, C. Liu, W. Yang, G. Zou, X. Zhang, F. Wu, S. Yu, X. Luo, X. Zhou, Naphthalimide derivatives as multifunctional molecules for detecting 5-formylpyrimidine by both PAGE analysis and dot-blot assays, Chem. Commun. 54(12) (2018) 1497-1500.

[49] L. Xu, Y.-C. Chen, J. Chong, A. Fin, L.S. McCoy, J. Xu, C. Zhang, D. Wang, Pyrene-based quantitative detection of the 5-formylcytosine loci symmetry in the CpG duplex content during TET-dependent demethylation, Angew. Chem. Int. Edit. 53(42) (2014) 11223-11227.

[50] T. Pfaffeneder, B. Hackner, M. Truß, M. Münzel, M. Müller, C.A. Deiml, C. Hagemeier, T. Carell, The discovery of 5-formylcytosine in embryonic stem cell DNA, Angew. Chem. Int. Edit. 50(31) (2011) 7008-7012.

[51] Y. Tang, S.-J. Zheng, C.-B. Qi, Y.-Q. Feng, B.-F. Yuan, Sensitive and simultaneous determination of 5-methylcytosine and its oxidation products in genomic DNA by chemical derivatization coupled with Liquid Chromatography-Tandem Mass Spectrometry analysis, Anal. Chem. 87(6) (2015) 3445-3452.

Graphical abstract